nature communications

Article

https://doi.org/10.1038/s41467-025-59121-6

# Acoustic loudness factor as an experimental parameter for benchmarking small molecule photoacoustic probes

Received: 15 May 2024

Accepted: 11 April 2025

Published online: 22 April 2025

Check for updates

Frederik Brøndsted[1,8,10], Julia L. McAfee[1,10], Jerimiah D. Moore[1], Harry R. Shield[1], Luca Menozzi[2], Xinqi Zhou[3,9], Yuan Fang[1], Ruwen Yin[1], Junjie Yao[2,4], Kelsey P. Kubelick[5] & Cliff I. Stains[1,6,7]

Photoacoustic imaging (PAI) is an emerging biomedical imaging modality with promise as a point-of-care diagnostic. This imaging modality relies on optical excitation of an absorber followed by production of ultrasound through the photoacoustic effect, resulting in high spatial resolution with imaging depths in the centimeter range. Herein, we disclose the discovery of the first benchmarking parameter for small molecule dye performance in PAI, which we term the acoustic loudness factor (ALF). ALF can predict dye performance in PAI without the need for access to photoacoustic instrumentation and can be used to guide the systematic evaluation of design strategies to enhance photoacoustic signal. Lastly, we demonstrate that enhancements in ALF can be translated to in vivo PAI. Akin to the use of fluorescence brightness in fluorophore design and evaluation for fluorescence imaging, we anticipate that ALF will guide the design and evaluation of improved probes for PAI.

The systematic design of robust small molecule imaging agents depends upon the existence of experimentally measurable benchmarking parameters that can be used to readily assess dye performance in vitro. The existence of such parameters enables the establishment of structure–activity relationships that can be used to increase dye performance in biological imaging applications[1]. In the context of fluorescence imaging, multiplication of the molar extinction coefficient (ε) by the quantum yield of fluorescence (Φ) yields a benchmarking parameter known as fluorescence brightness ($\Phi \times \varepsilon$)[2]. Indeed, fluorescence brightness has been used with great success to optimize the performance of fluorescent dyes in vitro for diverse applications in biological imaging[1,3–8].

PAI is an emerging biomedical imaging modality that combines the strengths of optical and ultrasound imaging, providing increased imaging depths in living organisms compared to fluorescence. The ability of PAI to provide non-invasive images of deep-tissue structures has already found applications in biomedical research and in the clinic[9,10]. While PAI relies on the optical excitation of an absorber, the signal readout is dependent upon the subsequent production of an ultrasound wave[9–13]. Ultrasound signal generation is caused by the use of pulsed laser excitation, which leads to thermoelastic expansion events arising from non-radiative decay of the absorber (Fig. 1). This phenomenon, known as the photoacoustic (PA) effect, was first described by Alexander Graham Bell in the 1880s[14]. Using pulsed near-infrared (NIR) excitation (660–1300 nm) affords imaging depths in the cm range, well beyond what is readily attainable with purely optical techniques. NIR-absorbing species including endogenous chromophores (e.g., hemoglobin), small-molecule dyes, inorganic nanoparticles, and reengineered fluorescent proteins have been utilized in PAI[15,16]. Among these, small-molecule dyes provide highly tunable

[1]Department of Chemistry, University of Virginia, Charlottesville, VA 22904, USA. [2]Department of Biomedical Engineering, Duke University, Durham, NC 27708, USA. [3]Department of Chemistry, University of Nebraska-Lincoln, Lincoln, NE 68588, USA. [4]Department of Neurology, Duke University School of Medicine, Durham, NC 27710, USA. [5]Department of Biomedical Engineering, University of Virginia, Charlottesville, VA 22908, USA. [6]University of Virginia Cancer Center, University of Virginia, Charlottesville, VA 22908, USA. [7]Virginia Drug Discovery Consortium, Blacksburg, VA 24061, USA. [8]Present address: Department of Biomedical Engineering, Oregon Health and Science University, Portland, OR 97201, USA. [9]Present address: Department of Chemistry, University of California, Berkeley, CA 94720, USA. [10]These authors contributed equally: Frederik Brøndsted, Julia L. McAfee. e-mail: cstains@virginia.edu

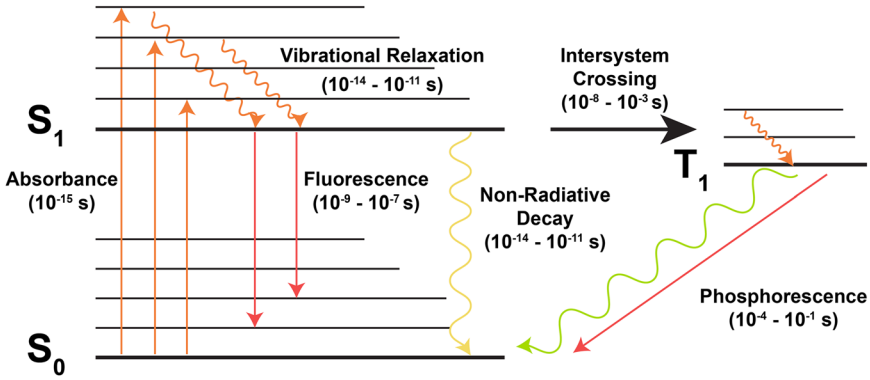


**Fig. 1 | Approximate timescales of various electronic transitions.** A Jablonski diagram showing the electronic transitions and approximate timescales for absorbance, fluorescence, intersystem crossing, phosphorescence, and non-radiative decay.

scaffolds for the construction of targeted contrast agents and molecular imaging probes[15–17], which provide biochemical information that is not accessible with endogenous chromophores. Despite the clear and emerging impact of PAI, no benchmarking parameters currently exist for predicting the performance of small molecule dyes in PAI. Previous studies have almost universally focused on repurposing fluorescent dyes with relatively poor Φ such as hemicyanine[17–21], boron dipyrromethene (BODIPY)[22–24], cyanine[25], and benzobisthiadiazole (BBTD) scaffolds[26] for PAI. However, recent work indicates that decreasing the Φ of a dye is not the sole driver of PA signal generation as absorbers with relatively high Φ can provide strong PA signal[27–29]. In the absence of a benchmarking parameter for predicting dye performance in PAI, the field lacks clear design principles for the enhancement of PA signal from small molecule dyes.

Under one-photon absorption conditions (i.e., low-intensity irradiation), PA signal generation is linear with respect to dye concentration and is described by Eq. 1[15]:

$$\rho = \varepsilon_g C_g \Gamma I \Phi_{nr} \tag{1}$$

Here $\rho$ is the pressure change, i.e., PA emission, $\varepsilon_g$ is the ground state molar absorption at the excitation wavelength, $C_g$ is the concentration of dye molecules in the ground state, Γ is the Grüneisen coefficient, $I$ is the incident photon fluence, and $\Phi_{nr}$ is the quantum yield of non-radiative decay. The Grüneisen coefficient, Γ, describes the medium's sound-conducting ability and is defined by Eq. 2:

$$\Gamma = \frac{V_s^2 \alpha}{C_p} \tag{2}$$

Where $V_s$ is the velocity of sound, α is the thermal expansion coefficient of the medium, and $C_p$ is the specific heat of the medium at constant pressure. From Eqs. 1 and 2, it becomes clear that the PA signal is influenced by the ability of a dye to absorb photons ($\varepsilon_g$), $\Phi_{nr}$, and the physical properties of the media described by Γ. Unlike Φ, which directly relates to radiative decay of the excited state via fluorescence emission (Fig. 1), $\Phi_{nr}$ is a complex parameter that can represent several different mechanistic pathways that lead to decreases in fluorescence, each of which may differentially influence PA signal output. The current practice of repurposing dyes with relatively low Φ for PAI assumes that any physical mechanism that decreases Φ will result in an increased PA signal. However, decreased Φ can result from several mechanisms, including intersystem crossing (ISC)[30–32], twisted intramolecular charge transfer[33], or internal conversion. Structural modifications such as auxochrome modifications[34], conformational restriction[22], or vibronic coupling[15,35] modulate non-radiative decay pathways and may differentially influence PA signal generation. Thus, while Eq. 1 provides important insight into physical factors that influence PA signal generation, it does not provide clear insight into design approaches that could be utilized to rationally tune PA signals. Rather, we argue that a benchmarking parameter that relates commonly measured photophysical properties of dyes such as ε, Φ, and fluorescence lifetime (τ) would enable efforts to rationally design improved dyes for PAI. Here we note that both Φ and τ depend on the radiative ($k_r$) and non-radiative ($k_{nr}$) decay rates of a dye, as shown in Eq. 3 (Fig. 1):

$$\Phi = \frac{k_r}{k_{nr} + k_r} \; and \; \tau = \frac{1}{k_{nr} + k_r} \tag{3}$$

This allows for the determination of $k_{nr}$ and $k_r$ from the measurable parameters of Φ and τ (Supplementary Note 1). Consequently, if PA intensity could be related to these readily observable experimental parameters, the influence of these photophysical properties on PA signal generation could be evaluated and employed to optimize dyes for PA output.

In this work, we screened a panel of structurally diverse dyes and correlate readily observable photophysical parameters to PA signal generation, resulting in the discovery of the first PA benchmarking parameter, which we term acoustic loudness factor (ALF). ALF is highly correlated to PA signal intensity ($R^2 = 0.9554$) and can be used to accurately predict PA signal generation from new dyes with a mean percent error (MPE) of 9.8%. With this new parameter in hand, we employed Bulky Alkyl Rotor (BAR) auxochromes, conformational restriction (CR), and asymmetry-induced vibronic coupling (AIVC) to modulate ALF, leading to new dye designs displaying more than 100% increases on an equal concentration basis as well as greater than 450% increases on a per photon basis in PA signal output. An optimal PA dye from these efforts, $NR_{773}$, was predicted by ALF to display a 97% increase in PA signal in vitro compared to a previously repurposed fluorescent dye described by our lab, $SNR_{700}$[36]. Indeed, as predicted, an increase in PA signal generation was observed in vitro as well as in living mice, demonstrating the ability to utilize ALF to optimize PA signal in vitro for subsequent applications in PAI. Taken together, this work provides the community with the first benchmarking parameter for comparison of PA dyes (akin to fluorescence brightness in the context of fluorescent dyes). ALF also enables the study of structure–activity relationships on PA signal without the need for access to PAI instrumentation. In the long term, we envision the use of ALF to construct dyes specifically designed for PAI, paving the way for the discovery of tailored agents for targeted as well as molecular PAI applications.

https://doi.org/10.1038/s41467-025-59121-6

a

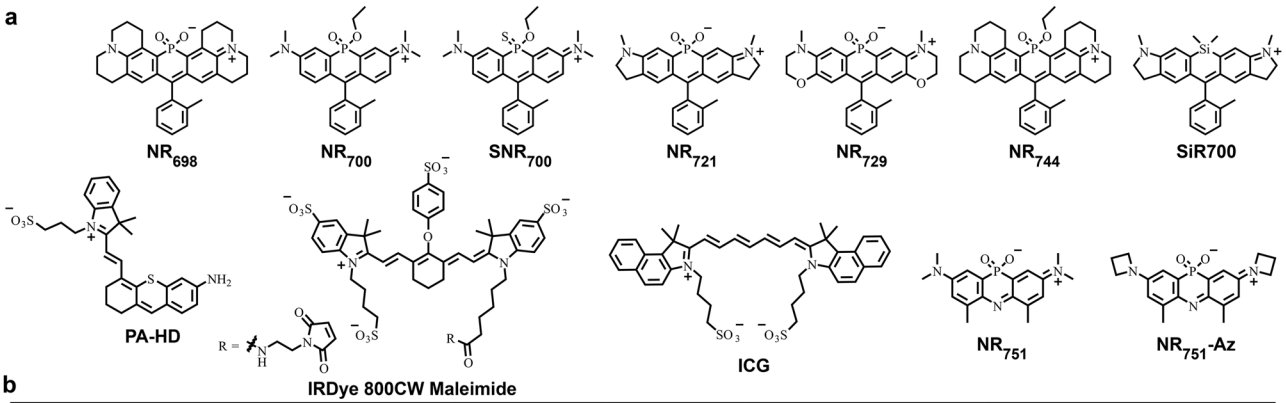


b

| Dyes | $\lambda_{abs}$ (nm) | $\lambda_{em}$ (nm) | ε ($M^{-1}cm^{-1}$) | Φ | τ (ns) | PABF ($M^{-1}cm^{-1}$) | $k_{nr}$ ($s^{-1}$) | $k_r$ ($s^{-1}$) | ALF ($M^{-1}cm^{-1}s^{-1}$) | Relative PA Intensity |
|---|---|---|---|---|---|---|---|---|---|---|
| $NR_{698}$ | 697 | 712 | 35,000 | 0.229 | 3.15 | 27,000 | 2.45E+08 | 7.26E+07 | 8.57E+12 | 0.36 |
| $NR_{700}$ | 700 | 722 | 71,000 | 0.124 | 1.84 | 62,200 | 4.76E+08 | 6.75E+07 | 3.38E+13 | 1.00 |
| $SNR_{700}$ | 701 | 734 | 92,400 | 0.055 | 1.83 | 87,300 | 5.16E+08 | 3.01E+07 | 4.77E+13 | 1.26 |
| $NR_{721}$ | 716 | 755 | 82,500 | 0.032 | 1.03 | 79,900 | 9.42E+08 | 3.10E+07 | 7.77E+13 | 1.23 |
| $NR_{729}$ | 727 | 786 | 54,600 | 0.029 | 5.20 | 53,000 | 1.87E+09 | 5.57E+07 | 1.02E+14 | 1.42 |
| $NR_{744}$ | 739 | 764 | 102,300 | 0.110 | 1.88 | 91,100 | 4.73E+08 | 5.85E+07 | 4.84E+13 | 1.11 |
| SiR700 | 694 | 722 | 82,300 | 0.262 | 2.52 | 60,800 | 2.93E+08 | 1.04E+08 | 2.41E+13 | 0.80 |
| $NR_{751}$ | 751 | 779 | 84,900 | 0.004 | 0.082 | 85,600 | 1.21E+10 | 4.73E+07 | 1.03E+15 | 3.51 |
| $NR_{751}$-Az | 747 | 768 | 115,000 | 0.006 | 0.092 | 114,300 | 1.08E+10 | 6.63E+07 | 1.24E+15 | 3.89 |
| PA-HD | 730 | 767 | 85,200 | 0.014 | 0.20 | 84,000 | 4.90E+09 | 7.01E+07 | 4.18E+14 | 3.12 |
| ICG | 783 | 820 | 273,000 | 0.075 | 0.31 | 252,700 | 2.98E+09 | 2.42E+08 | 8.14E+14 | 3.49 |
| IRDye 800CW | 777 | 798 | 338,200 | 0.097 | 0.60 | 305,500 | 1.51E+09 | 1.61E+08 | 5.10E+14 | 4.00 |

c

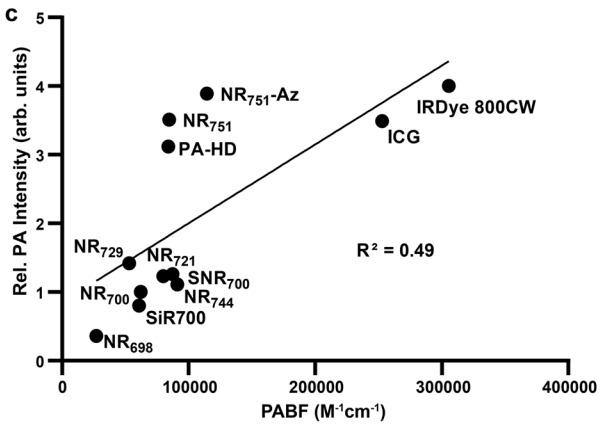


d

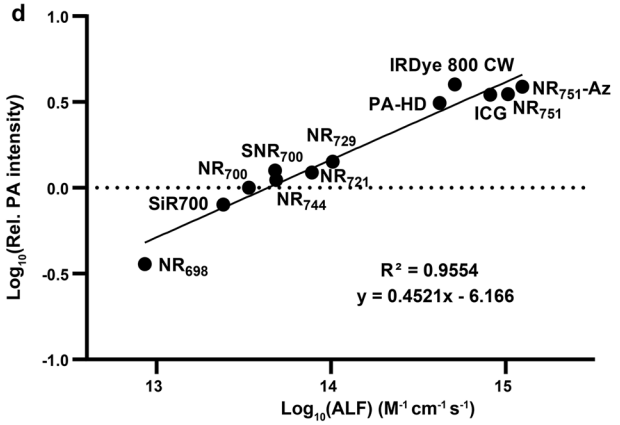


**Fig. 2 | Discovery of the acoustic loudness factor.** Structures (**a**) and photophysical properties as well as PA intensities (**b**) for a panel of structurally diverse NIR dyes. Relative PA emission intensity plotted versus photoacoustic brightness factor (PABF) (**c**) or acoustic loudness factor (ALF) (**d**). Trendlines represent fits from linear regression. Photophysical properties were measured in triplicate in DPBS:MeCN (7:3, 1% DMSO). PA emission is from quantification of PA images of 1.2 cm thick tissue phantoms at positions 2 mm apart.

## Results and discussion

### Discovery of the acoustic loudness factor

Our lab has a longstanding interest in the development of far-red and NIR phosphinate-containing dyes, termed Nebraska Red (NR) dyes, for applications in chemical biology[36–42]. More recently, we have shown that NR dyes are capable of producing PA signal[36,41]. Having a panel of NR dyes at our disposal (Fig. 2a)[36,37,41,42], we sought to identify experimentally observable parameters that correlate to PA signal output. To accomplish this goal, we first screened solvent conditions for PAI in FEP tubes within 1.2 cm thick tissue phantoms consisting of 5% agarose (w/v) and 2.5% milk (v/v). This is an important first step as it allows for direct comparison of PA signal produced from dyes in the absence of confounding factors such as solubility which is often problematic for NIR dyes[15,43]. Using $NR_{700}$ as a test case, we performed PAI in DPBS (1% DMSO) or a mixed solvent system consisting of DPBS and acetonitrile (7:3 DPBS:MeCN, 1% DMSO). Samples in DPBS showed uneven PA signal distribution, displaying a donut pattern with the highest intensity at the surface of the FEP tube, whereas the mixed DPBS/MeCN solvent system afforded a homogenous PA signal throughout the FEP tube (Fig. S1). We hypothesize that the donut pattern seen in DPBS was due to the interaction of the dye with the FEP tubing. To alleviate these effects, all subsequent measurements of PA intensity and photophysical properties (ε, Φ, and τ) were performed in the 7:3 DPBS:MeCN mixed solvent system (Fig. 2b).

Having established the photophysical properties and PA signal intensity of our previously published NR dyes at 10 μM in the optimized solvent system, we initially sought to plot PA intensity versus the previously described photoacoustic brightness factor (PABF, Eq. 4),

which has been used to assess the potential performance of small molecule dyes in PAI[22].

$$\mathrm{PABF} = (1-\Phi) * \varepsilon = \left(\frac{k_{nr}}{k_{nr}+k_r}\right) * \varepsilon \quad (4)$$

For this, and subsequent analyses, PA signal measurements are reported relative to $NR_{700}$ since this was the first NR dye with confirmed PA activity[36]. Surprisingly, very little correlation was found between PABF and the PA intensity of NR dyes in our panel (Fig. S2). To further investigate the influence of dye structure on PABF, we added silicone rhodamine (SiR700)[44], hemicyanine (PA-HD)[20], oxazine ($NR_{751}$ and $NR_{751}$-Az)[41], and cyanine dyes (IRDye 800CW Maleimide and Indocyanine Green – ICG) to our panel (Fig. 2a, b). The inclusion of these structurally diverse dyes resulted in a moderate improvement in the correlation of PA intensity to PABF ($R^2 = 0.61$, Fig. 2c). Thus, while PABF represents an important step towards a benchmarking parameter that can predict the PA intensity of dyes, more work is needed to fully capture the influence of structural modifications on PA intensity.

From the above discussion of Eqs. 1 and 3 as well as previous investigations of PA probes[27–29], we surmised that the rates of radiative ($k_r$) and non-radiative ($k_{nr}$) decay for NIR dyes may play an important role in the development of a benchmarking parameter. Measuring these rates across our dye panel, we noticed that $k_{nr}$ trended toward being an order of magnitude larger than $k_r$ (Fig. 2b). Expansion of PABF (Eq. 4) to include these rates provides insight into why this term likely leads to poor correlations with PA intensity for NIR dyes. Specifically, as $k_{nr}$ becomes larger than $k_r$ the rate component of PABF approaches 1, meaning that PABF is driven largely by changes in ε for dyes with relatively large $k_{nr}$ (as is generally the case for NIR dyes[45], Fig. 2c). Based on these observations and previous work[28,29], we hypothesize that $k_{nr}$ should contribute significantly to PA signal generation of NIR dyes. Accordingly, we sought to develop a benchmarking parameter that would give ε and $k_{nr}$ equal weighting. Gratifyingly, after some trial and error, we found a strong linear correlation between the $\log_{10}$ of PA intensity and $\log_{10}$ of $k_{nr}$*ε for our dye panel ($R^2 = 0.9554$, Fig. 2d). Herein, we define $k_{nr}$*ε as the acoustic loudness factor (ALF, Eq. 5).

$$\text{Acoustic Loudness Factor} = k_{nr} * \varepsilon \quad (5)$$

Importantly, ALF provides equal weighing to both ε and $k_{nr}$ allowing for comparison of dyes with relatively large $k_{nr}$ compared to $k_r$, as is generally the case for NIR dyes[45]. Notably, ALF (Eq. 5) aligns with the theoretical framework of Eq. 1, incorporating both photon absorbance (ε vs $\varepsilon_g$) and energy conversion efficiency ($k_{nr}$ vs $\Phi_{nr}$). Here, we note that ALF correlates with signal output measured from 8 to 10 ns laser excitation pulses, where the signal depends on the rate of non-radiative decay ($k_{nr}$) rather than the fraction of decay via non-radiative pathways ($\Phi_{nr}$). This suggests that dyes with faster $k_{nr}$ would produce stronger PA signals, since more rapid excitation-relaxation cycles within the timeframe of the laser excitation pulse would generate greater overall PA output[28]. Lastly, the generality of ALF across PAI instrumentation was examined using a custom-built 3D scanning linear-array system[46] and a commercial VisualSonics instrument from Fujifilm. Here again, we observed a strong correlation between $\log_{10}$ of PA intensity and $\log_{10}$ of ALF (Figs. S3, S4, $R^2 \geq 0.987$), highlighting the applicability of ALF across different PAI setups with different types of transducers.

Investigation of this new benchmarking parameter clearly indicates that maximization of ALF should lead to increased PA signal. This can be accomplished through two pathways, maximization of ε or maximization of $k_{nr}$. Since several approaches exist for increasing ε in small molecule dyes[22,47], we instead chose to focus on structural modifications aimed at increasing $k_{nr}$. In particular, we view efforts to define $k_{nr}$ pathways that lead to increased PA signal as paramount since our data (see below) as well as previous work[43] indicates that not all non-radiative decay pathways lead to observable PA signal on current PAI instrumentation. Thus, we sought to examine whether modulation of $k_{nr}$ through triplet state decay, BAR[48–50], CR[22], or AIVC[51] would produce changes in ALF that could predict the relative PA intensity of new dyes.

## Non-radiative decay from the triplet state

Non-radiative decay from the singlet excited state is generally assumed to be the driver of PA output on current commercial instrumentation, which utilizes laser pulses in the ~ns timescale with ~10 Hz repetition rates[28,29]. However, methylene blue displays an unusually short-lived triplet state (~ns) that leads to productive PA signal generation under these instrumental parameters[43,52]. These observations highlight the need to investigate different mechanisms of $k_{nr}$ and their contribution to PA signal generation. To examine the contribution of non-radiative decay of the triplet state to PA signal generation in NR dyes, $NR_{700}$ was chosen since Fig. 2d indicates the potential to improve the PA signal of this dye relative to other NR derivatives. We chose to induce intersystem crossing (ISC) and modulate $k_{nr}$ through the well-established collisional quenching of rhodamine dyes by potassium iodide (KI)[32,53]. Previous work has shown a concentration-dependent fluorescence quenching of dyes by KI via an external heavy atom effect[32] that modulates the rate of intersystem crossing[2,30–32]. To test this, the photophysical properties of $NR_{700}$ in DPBS (1% DMSO) in the presence of increasing concentrations of KI (0–500 mM) were measured. Here, DPBS was selected as the solvent of choice to ensure full solubility of KI. As expected, KI addition quenched the fluorescence, decreased Φ and fluorescence lifetime, and linearly increased $k_{nr}$, while ε remained stable regardless of the concentration of KI (Fig. 3a, Fig. S5, and Table S1). The increase in $k_{nr}$ reflects the intermolecular interactions between $NR_{700}$ and $I^-$. Based on the increase in $k_{nr}$ of 528% over this concentration range, ALF would predict a corresponding increase of 134% in the PA signal. However, we found that while KI addition linearly increased $k_{nr}$, PA signal decreased over the same range of KI concentrations (Fig. 3b). This observation suggests that promoting ISC is counterproductive under these experimental conditions. Since previous reports have demonstrated PA signal generation arising from the non-radiative decay of the methylene blue triplet state[43,52], one plausible explanation for our observation could be a mismatch between the relatively longer triplet lifetime of rhodamine dyes (>1 μs)[53] and the PAI instrumentation used here. Indeed, the PAI instrumentation used here (iTheraMedical 256-TF MSOT) employs 8–10 ns laser pulses with 10 Hz repetition rates, rendering dyes with excited state lifetimes >50 ns effectively "invisible" due to the temporal gap between excitation and PA signal generation. The unintuitive observation of decreased PA signal with increasing [KI] seen in Fig. 3b could be due to ground-state depopulation (due to more efficient ISC) at higher KI concentrations. We note that with the addition of 500 mM KI, a slight recovery of the PA signal is observed. This could be due to shortened triplet state lifetimes at high [KI], which has been observed for other rhodamine dyes[32]. However, more studies are required to definitively determine the origin of this increase at high [KI].

Based on the data presented above, we caution the reader to interpret $k_{nr}$ in ALF (Eq. 5) as non-radiative decay from the singlet excited state when correlating ALF to PA output on current commercial PAI instrumentation. When using dyes with long-lived triplet states or working in complex environments where decay rates are dependent on interactions between multiple molecules, caution should be taken when correlating PA output and ALF.

## Bulky alkyl rotor dyes

We chose to investigate BAR since modifications of this type have been shown to increase non-radiative relaxation of the excited state[50,54,55]. A series of BAR-modified NR dyes bearing *N*-isopropyl, -cyclopentyl, or

https://doi.org/10.1038/s41467-025-59121-6

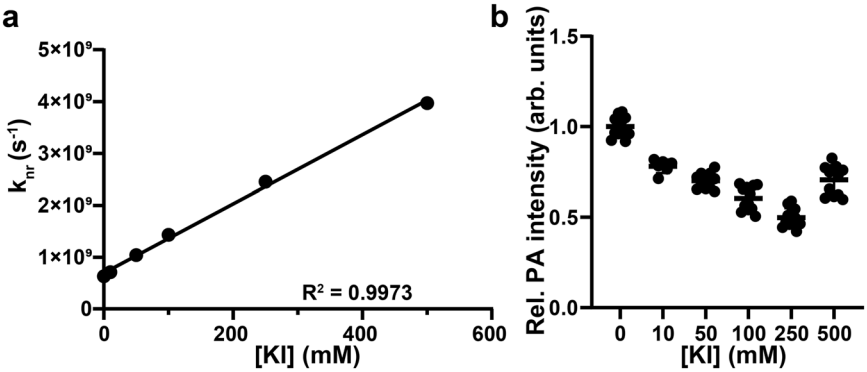


**Fig. 3 | Promoting ISC does not result in increased PA signal from $NR_{700}$. a** Non-radiative decay rate plotted versus concentration of potassium iodide. The trend line was obtained using linear regression. **b** Photoacoustic emission intensity plotted versus concentration of potassium iodide. Photophysical properties used to calculate $k_{nr}$ were measured in DPBS (1% DMSO). PA emission was from quantification of PAI in DPBS (1% DMSO) in 1.2 cm thick tissue phantoms at positions 2 mm apart (mean ± SD, 0, 100, 250, and 500 μM $n = 12$, 10 μM $n = 11$, 50 μM $n = 6$).

-cyclohexyl auxochromes were synthesized. In short, two subsequent reductive aminations were used to install the BAR motif, followed by methylation of the amine. Next, an acid-catalyzed condensation yielded a dimer structure from which a phosphorous-bridged xanthone was fashioned using organolithium chemistry. The final products, $NR_{706}$-iPr, $NR_{716}$-Cp, and $NR_{716}$-Ch were obtained by installation of the pendant phenyl ring through an additional lithium-halogen exchange reaction (Fig. 4a, Figs. S6, S7, and Supplementary Materials). Interestingly, modification of NR dyes with BAR increased both the ε and $k_{nr}$ of the resulting dyes relative to $NR_{700}$ (Fig. 4c), giving ALF values as high as $1.49 \times 10^{14}$ $M^{-1}cm^{-1}s^{-1}$ (compared to $3.38 \times 10^{13}$ $M^{-1}cm^{-1}$ for $NR_{700}$).

Signal generation efficiency (SGE) and molar signal generation efficiency (MSGE) have been commonly used to compare the ability of dyes to convert absorbed photons into PA signal[28]. SGE is reported as a PA signal normalized to the ε of each dye (see Supplementary Materials) and reflects the efficiency of PA signal generation per photon absorbed. MSGE compares PA output at equal dye concentrations (10 μM here) and can be used to identify probe scaffolds for in vivo applications, where dosing and photon budget are limited. The SGE of BAR-modified dyes was comparable to $NR_{700}$ (Fig. 5a). However, MSGE revealed 49, 114, and 51% increases in PA signal for $NR_{706}$-iPr, $NR_{716}$-Cp, and $NR_{716}$-Ch relative to $NR_{700}$, consistent with predictions based on ALF (Figs. 4b, c, 5b). These results show that BAR modifications do not enhance PA efficiency per photon (SGE) but improve MSGE by increasing both ε and $k_{nr}$, the components of ALF. We propose that MSGE improvements are critical for PAI, as agents with high MSGE provide better signal-to-noise ratios and require lower doses to achieve sufficient contrast. This underscores the value of ALF as a predictive benchmark for PA probes and its utility in designing imaging agents for PAI applications.

## Conformationally restricted dyes

Previous work from Chan and colleagues has shown that CR can lead to an increase in PA output of aza-BODIPY dyes[22]. This effect is perhaps counterintuitive since CR can often lead to an increase in Φ, further highlighting issues surrounding the current approach of simply decreasing Φ to improve the PA signal and reinforcing the need for a PA benchmarking parameter. Thus, we sought to test the influence of CR on PA output in NR dyes. Interestingly, two previously described dyes from our lab, $NR_{721}$ and $NR_{729}$[42], contain CR modifications and showed increased PA emission compared to $NR_{700}$ that is primarily driven by increased $k_{nr}$ (Fig. 2a, b). We sought to further investigate this effect in the context of phosphinate ethyl ester containing dyes to provide a more direct comparison to $NR_{700}$. Thus, we synthesized phosphinate ethyl ester derivatives of $NR_{721}$ and $NR_{729}$, termed $NR_{773}$ and $NR_{778}$ (Fig. 4a, Figs. S6, S7, and Supplementary Material). In addition, we synthesized an analog of $NR_{778}$ with CR at the ortho-position relative to the heteroatom bridge, termed $NR_{702}$, as well as the corresponding azaphosphinate derivative $NR_{746}$ (Fig. 4a, Figs. S6, S7, and Supplementary Material). Both $NR_{773}$ and $NR_{778}$ displayed increased $k_{nr}$, however the ε of $NR_{778}$ decreased by 54% relative to $NR_{700}$ (Fig. 4c). On a per photon basis $NR_{773}$ and $NR_{778}$ were 119 and 330% more efficient at generating PA signal compared to $NR_{700}$ (SGE, Fig. 5a). When comparing equal concentrations of dye (MSGE), PA signals were enhanced by 123 and 97% for $NR_{773}$ and $NR_{778}$ compared to $NR_{700}$, as predicted by ALF (Fig. 4b, c). The associated increase in PA emission of these dyes is driven by increased $k_{nr}$, and the improved MSGE of $NR_{773}$ is driven by the maintenance of relatively high ε compared to $NR_{778}$. Alternatively, measurement of the photophysical properties of $NR_{702}$ yielded an increased ε but decreased $k_{nr}$ by 45% relative to $NR_{700}$ (Fig. 4c). Thus, the per photon efficiency of PA generation from $NR_{702}$ was severely decreased compared to $NR_{700}$ (Fig. 5a). However, $NR_{702}$ displayed virtually identical PA emission on an equal concentration basis due to its high ε, as predicted by ALF (Figs. 4b, c, 5b). $NR_{746}$ contains the same CR modification compared to $NR_{702}$ but on the azaphosphinate scaffold (Fig. 4) and displayed a modest 16% increase in SGE relative to $NR_{700}$ (Fig. 5a). However, $NR_{746}$ displayed a robust 174% increase in MSGE, as predicted by ALF (Figs. 4b, c, 5b), compared to $NR_{700}$. This observation reinforces the potential of azaphosphinates as loud PA probes (Fig. 2)[41]. These results indicate that PA enhancements from CR are position-dependent and again highlight the utility of ALF for guiding the investigation of structure–activity relationships in the context of PA signal generation.

## Dyes with asymmetry-induced vibronic coupling

We next investigated the influence of AIVC on ALF and PA signal output in NR dyes since our previous studies have shown that increased vibronic coupling can increase PA signal from heteroatom xanthenes[35]. Driven by the observed increases in MSGE via CR, we designed the asymmetric dyes $NR_{727}$ and $NR_{735}$ using a modular synthetic route (Fig. 4a, Figs. S6, S7, and Supplementary Material). In addition, we synthesized a hybrid dye containing both indoline and morpholino auxochromes, termed $NR_{759}$ (Fig. 4a and Supplementary Material). All three dyes displayed an increased Stokes shift relative to $NR_{700}$, indicating the presence of increased vibronic coupling. We also observed an increase in Stokes shift with increasing absorbance wavelength within this series. Unfortunately, the Φ and τ of $NR_{759}$ were too low to be measured, which prohibited experimental determination of $k_{nr}$. Nonetheless, by rearranging the ALF trend line from Fig. 2d, we were able to estimate the $k_{nr}$ of $NR_{759}$ as $6.39 \times 10^9$ $s^{-1}$(Fig. 4c and Supplementary Note 2). Although AIVC generally reduced the ε for dyes in this series, the $k_{nr}$ was increased for $NR_{727}$ (220%), $NR_{735}$ (1290%), and $NR_{759}$

https://doi.org/10.1038/s41467-025-59121-6

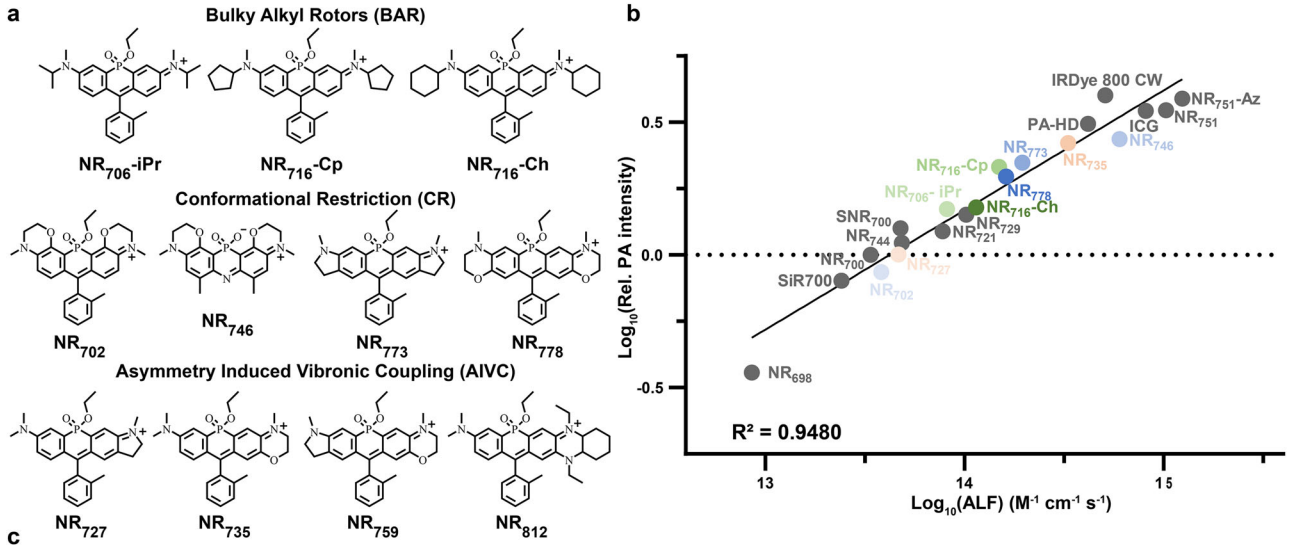


c

| Design Strategy | Dyes | $\lambda_{abs}$ (nm) | $\lambda_{em}$ (nm) | ε ($M^{-1}cm^{-1}$) | Φ | τ (ns) | $k_{nr}$ ($s^{-1}$) | ALF ($M^{-1}$ $cm^{-1}$ $s^{-1}$) | Relative PA Intensity | Predicted Rel. PA Intensity | Percentage Error (%) |
|---|---|---|---|---|---|---|---|---|---|---|---|
| | $NR_{700}$ | 700 | 722 | 71,000 | 0.124 | 1.84 | 4.76E+08 | 3.38E+13 | 1.00 | - | - |
| BAR | $NR_{706}$-iPr | 706 | 738 | 114,600 | 0.073 | 1.30 | 7.13E+08 | 8.18E+13 | 1.49 | 1.33 | 10.75 |
| | $NR_{716}$-Cp | 716 | 750 | 129,000 | 0.041 | 0.83 | 1.16E+09 | 1.49E+14 | 2.14 | 1.75 | 18.59 |
| | $NR_{716}$-Ch | 716 | 748 | 123,600 | 0.047 | 1.03 | 9.26E+08 | 1.14E+14 | 1.51 | 1.55 | 2.40 |
| CR | $NR_{702}$ | 700 | 715 | 145,100 | 0.210 | 3.00 | 2.63E+08 | 3.82E+13 | 0.86 | 0.94 | 9.30 |
| | $NR_{746}$ | 745 | 763 | 167,900 | 0.012 | 0.28 | 3.58E+09 | 6.01E+14 | 2.74 | 3.28 | 19.65 |
| | $NR_{773}$ | 769 | 812 | 71,700 | 0.023 | 0.36 | 2.72E+09 | 1.95E+14 | 2.23 | 1.97 | 11.67 |
| | $NR_{778}$ | 781 | 833 | 32,600 | 0.001 | 0.20 | 4.97E+09 | 1.62E+14 | 1.97 | 1.81 | 8.25 |
| AIVC | $NR_{727}$ | 727 | 762 | 31,000 | 0.038 | 0.64 | 1.51E+09 | 4.67E+13 | 1.00 | 1.03 | 2.86 |
| | $NR_{735}$ | 735 | 793 | 50,000 | 0.004 | 0.15 | 6.64E+09 | 3.32E+14 | 2.64 | 2.51 | 5.10 |
| | $NR_{759}$ | 757 | 826 | 21,500 | - | - | 6.66E+09[b] | - | 1.71 | - | - |
| | $NR_{812}$ | 828 | 1012[a] | 24,700 | 0.002[a] | - | 8.00E+09[b] | - | 1.98 | - | - |

**Fig. 4 | ALF can be used to predict PA intensity. a** Structures of new NR dyes used to investigate the ability of acoustic loudness factor (ALF) to predict changes in PA signal derived from different mechanisms of modulating $k_{nr}$. **b** Dyes from panel a plotted on the trend line from Fig. 2d. **c** Photophysical properties and predicted PA intensities from dyes shown in panel a. Photophysical properties were measured in triplicate in DPBS:MeCN (7:3, 1% DMSO). PA emission was measured from quantification of PA images of 1.2 cm thick tissue phantoms at positions 2 mm apart ($n > 5$). [a]Dichloromethane used as a solvent. [b]Non-radiative decay rates are calculated from the ALF trend line in Fig. 2d (Supplementary Note 2).

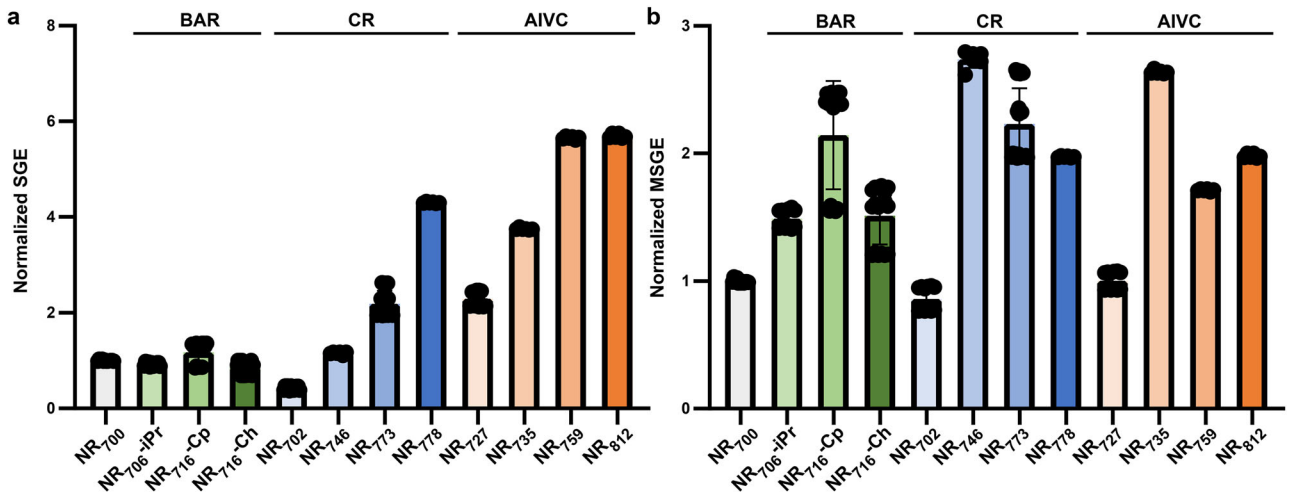


**Fig. 5 | Comparison of photoacoustic signal generation efficiencies for different design strategies. a** Per photon signal generation efficiency (SGE) for new dyes relative to $NR_{700}$. **b** Normalized molar signal generation efficiency (MSGE) of new dyes relative to $NR_{700}$. PA signal was quantified from PA images of 1.2 cm thick tissue phantoms at positions 2 mm apart (mean ± SD, $NR_{735}$, $NR_{746}$, $NR_{759}$, $NR_{778}$, and $NR_{812}$ $n = 6$, $n = 12$ for $NR_{700}$, $NR_{702}$, $NR_{727}$, and $NR_{706}$-iPr, $n = 18$ for $NR_{716}$-Cp and $NR_{716}$-Ch, and $n = 24$ for $NR_{773}$).

(1300%) relative to $NR_{700}$ (Fig. 4c). The effect of increased $k_{nr}$ is seen in the increased per photon efficiency of PA emission from these dyes (SGE, Fig. 5a). At equal concentrations, $NR_{727}$ is predicted by ALF to produce equivalent PA signal to $NR_{700}$ due to decreased ε, which was observed experimentally (Figs. 4b, c, 5b). Due to its relatively high ε alongside the highest $k_{nr}$ in our panel, ALF predicts a substantially increased PA signal from $NR_{735}$ compared to $NR_{700}$ (Figs. 4b, c, 5b). Indeed, this improvement in PA performance at equal concentration was verified by the observation of a 164% increase in signal from $NR_{735}$ compared to $NR_{700}$ (Figs. 4c, 5b). Although ALF for $NR_{759}$ could not be determined experimentally due to the low Φ and τ of this dye, we observed a modest 71% improvement in PA signal output at equal concentrations relative to $NR_{700}$, due to the relatively low ε of this dye (Fig. 4c).

To further investigate the effect of large AIVC on PA signal generation in NR dyes, we chose to utilize an approach to induce large Stokes shifts in fluorescent dyes that was described by Zhang and colleagues[51]. This strategy employs the 1,4-diethyl-decahydro-quinoaline (DQ) motif to afford asymmetric dyes with significant Stokes shifts and broad absorbance peaks, due to vibronic coupling. Accordingly, we synthesized an NR dye bearing the DQ motif, termed $NR_{812}$ (Fig. 4a and Supplementary Material). $NR_{812}$ represents the reddest NR dye to date, displaying an absorbance maximum of >800 nm (Fig. 4c and Fig. S5). As predicted, an exceptionally large Stokes shift of 184 nm was observed in DCM, yielding a fluorescence maximum at 1012 nm (Fig. 4c and Fig. S8). Since the Φ and τ for $NR_{812}$ in the mixed solvent system were too low for determination of ALF, we again utilized the rearranged form of the trend line in Fig. 2d (see Supplementary Note 2) to estimate $k_{nr}$ as $7.61 \times 10^9\ s^{-1}$ (Fig. 4c). Based on this, we would predict an enhanced per photon PA signal (SGE) from $NR_{812}$ versus $NR_{700}$, which was observed when PA signal intensities were normalized for ε (Fig. 5a). Nonetheless, when normalized to concentration, we would predict that the observed decrease in ε of $NR_{812}$ would counterbalance the effect of increased $k_{nr}$, leading to a muted enhancement in PA signal relative to $NR_{700}$. This prediction is again supported by experimental observation, where $NR_{812}$ produces 98% more PA signal than $NR_{700}$ at equal concentrations (Fig. 5b) but underperforms other dyes investigated in this work. Here again, efforts to restore the ε of $NR_{812}$ while maintaining $k_{nr}$ would be expected to enhance the performance of this dye on an equal concentration level. However, we note that the introduction of the DQ motif results in a very broad absorbance spectrum that may complicate imaging deconvolution using multispectral unmixing analysis. Overall, considering the MSGE of the AIVC dye series (Fig. 5b), we view AIVC modifications as promising approaches for PA probe design, due to their ability to maintain relatively high ε while also increasing $k_{nr}$. Our lab is currently pursuing dyes that may synergistically incorporate effects observed in BAR, CR, and AIVC to further improve PA signal generation in small molecule dyes. Our lab is also actively investigating whether ALF is applicable to metal nanoparticles commonly used in PAI.

### Enhancements in ALF are translatable to in vivo PAI

Since higher molar PA intensity is desirable for targeted as well as molecular PAI agents, we used ALF to identify lead candidates for in vivo PAI. This is because, for in vivo imaging, signal-to-noise will be dependent upon the concentration of the retained sensor at a particular site or PA active product produced after reaction with a target analyte. Importantly, we have clearly demonstrated that ALF can be used to predict relative differences in PA intensity for small molecule dyes at equal concentrations, even in the absence of PA instrumentation (Figs. 2d, 4c). Since we have previously demonstrated that azaphosphinates produce loud PA signal[41], we focused on rhodamine dyes with the largest ALF improvement from the BAR ($NR_{716}$-Cp), CR ($NR_{773}$), and AIVC ($NR_{735}$) panels as lead candidates for in vivo imaging. Interestingly, these dyes do not always display the lowest Φ within their respective series but do provide the highest enhancements in ALF relative to $NR_{700}$ of 340 ($NR_{716}$-Cp), 480 ($NR_{773}$), and 880% ($NR_{735}$, Fig. 5b). These observations reinforce the need for a PA benchmarking parameter that can be used to evaluate dye performance in PAI.

We next turned our attention towards in vivo stability of these phosphinate-containing dyes. We have previously shown that phosphinate ester dyes can undergo hydrolysis at physiological pH to afford the corresponding phosphinate dye[37–39] and that this hydrolysis event can be undesirable for PAI due to changes in the photophysical properties of the resulting hydrolyzed dye[36]. In addition, phosphinate ester dyes are generally able to cross cell membranes while phosphinate dyes cannot[36–40]. Therefore, we tested the chemical stability of our lead phosphinate ethyl ester dyes at relevant biological pH. These experiments showed that $NR_{773}$ displayed the slowest hydrolysis and was stable over the time required for in vivo imaging in this study (Fig. S9). Although the fluorescence of $NR_{773}$ is relatively dim, we were able to verify its ability to cross the cell membrane using confocal fluorescence microscopy (Fig. S10). Lastly, we did not observe cellular toxicity from $NR_{773}$ at relevant concentrations used for imaging (Fig. S11). In light of these results, we chose $NR_{773}$ for further evaluation in in vivo PAI.

To assess whether enhancements in ALF are translatable to in vivo PAI, we chose to compare $NR_{773}$ to $SNR_{700}$, a hydrolytically stabilized version of $NR_{700}$ that was previously developed by our lab (Figs. 2, 4, 6a)[36]. $SNR_{700}$ or $NR_{773}$ were subcutaneously injected into the left or right flanks of live mice, respectively, and the mice were scanned translationally across the length of the animal (from chest to hips). Multispectral unmixing was utilized to differentiate the dye signal from the endogenous absorbers oxyhemoglobin ($HbO_2$) and hemoglobin (Hb). Although the distribution of each dye was influenced by physical properties such as water solubility, we were able to identify a region of interest (ROI) for both agents using a red/blue/black filter (Fig. S12). Spectral unmixing verified that these ROIs represented signals from each dye (Fig. 6b–d). In addition, the change in integrated PA intensity versus wavelength also clearly supported the identity of each dye within their respective ROI (Fig. S13). Quantification of the integrated pixel intensity yielded a 590% increase, on average, in PA intensity for $NR_{773}$ relative to $SNR_{700}$ (Fig. 6e and Supplemental Movie 1). This increase exceeds the observed 123% increase in PA signal from $NR_{773}$ compared to $SNR_{700}$ in vitro (Figs. 2b, 4c), potentially due to differences in photophysical properties of the dyes in the respective in vitro and in vivo environments. Here, it is important to note that, like fluorescence brightness, changes in ALF are solvent-dependent since the photophysical parameters used to determine each benchmarking parameter are dependent upon solvent. Therefore, the reader is cautioned that changes in ALF may not always translate between conditions in which different solvents are used and should only be directly compared within the same solvent system (as is the case with fluorescence brightness). Other factors, including cell permeability and water solubility, may further impact in vivo performance. Lastly, we examined the clearance of $NR_{773}$ after administration using a tail vein catheter. Time-lapsed PAI revealed perfusion of dye through the cortex of the kidneys to the renal pelvis (Supplemental Movie 2), with the dye ultimately clearing to the bladder (Fig. S14). Taken together, these results demonstrate the potential of $NR_{773}$ for in vivo PAI and highlight the ability of ALF to guide the design of probes for use in living organisms.

Herein, we described the discovery of ALF, the first parameter for benchmarking the performance of small molecule dyes in PAI. Importantly, we showed that this parameter is capable of predicting PA signals without the need for access to PA instrumentation. We showed that ALF is capable of predicting the relative PA intensity of a wide range of dyes used in in vivo PAI, including cyanines, hemicyanines, oxazine derivatives, and xanthenes. ALF clearly predicts that increases in $k_{nr}$ and/or ε will lead to improved PA signal output for a dye scaffold,

https://doi.org/10.1038/s41467-025-59121-6

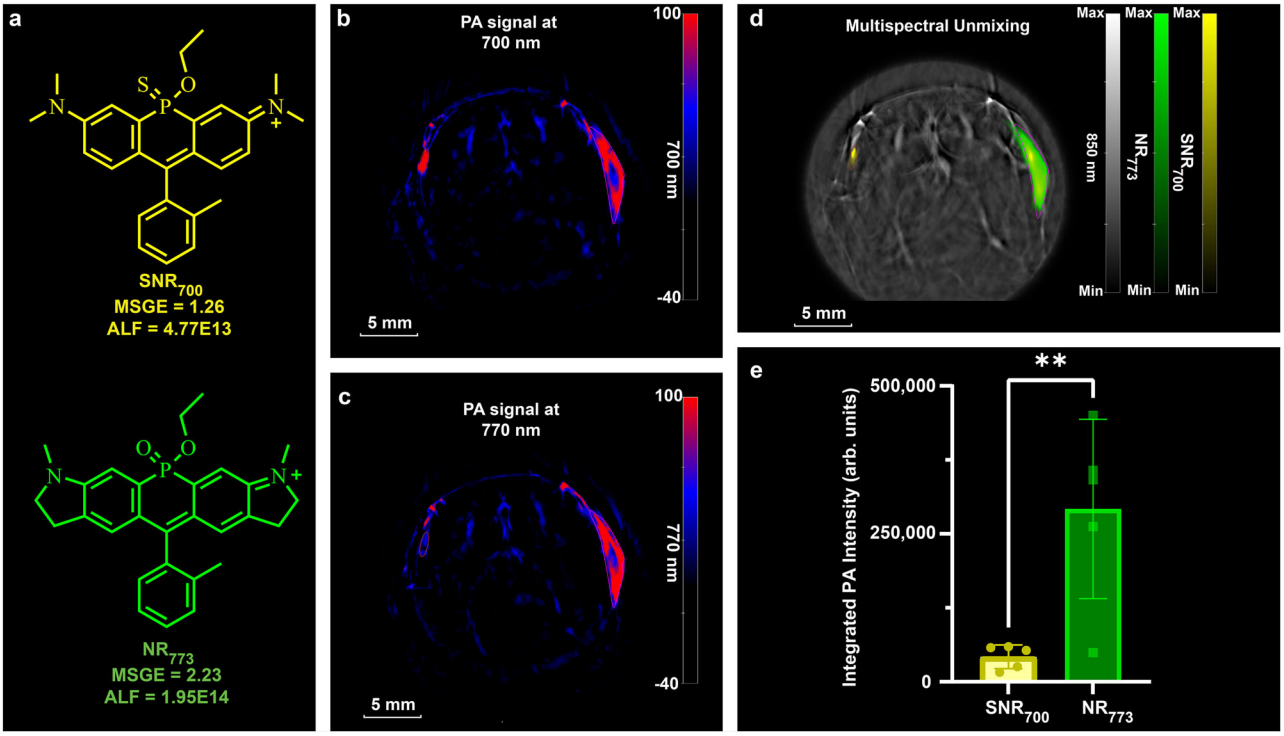


**Fig. 6 | Enhancements in ALF are translatable to in vivo PAI. a** Structures, MSGE values, and ALF values for $SNR_{700}$ and $NR_{773}$ used for in vivo comparison. Cross-sectional PA images in the x-y plane for mice subcutaneously injected with $SNR_{700}$ (left flank) or $NR_{773}$ (right flank) at 700 nm and **c** 770 nm using a red/blue/black color mask. Dyes were administered at 10 nmol in saline containing 2% DMSO and animals ($n = 5$) were imaged after 10 min. **d** Greyscale photoacoustic background image at 850 nm overlaid with multispectral unmixing attribution of $SNR_{700}$ (left flank) and $NR_{773}$ (right flank). ROIs identified from panels **b**, **c** are shown for comparison. **e** Comparison of integrated PA intensities for $SNR_{700}$ (mean = 42,321 ± 20,095) and $NR_{773}$ (mean = 292,103 ± 151,305) within ROIs defined by the red/blue/black color masks (panels b, c and Fig. S12) corresponding to each dye for five different mice. Error bars = SD. Statistical analysis was performed using a two-tailed *t*-test (**indicates a *p* value of <0.01, $p = 0.0064$). Yellow shading represents $SNR_{700}$ and green shading represents $NR_{773}$.

prompting an investigation of the influence of different mechanisms for modulating $k_{nr}$ on PA signal output. First, we demonstrated that non-radiative decay from the triplet state does not lead to productive PA signal output for xanthene dyes using current commercial instrumentation. Next, we investigated the influence of (1) bulky alkyl rotors, (2) conformational restriction, and (3) asymmetry-induced vibronic coupling on PA signal for a series of 11 previously unreported NIR dyes. In all cases, ALF was able to accurately predict changes in PA signal (MPE = 9.8%) due to structural modifications. Using these approaches, we were able to obtain rhodamine-based dyes with enhancements of 164% in MSGE ($NR_{735}$) and 459% in SGE ($NR_{812}$) compared to our initial probe $NR_{700}$. Finally, we demonstrate that increases in ALF observed in vitro can be translated to in vivo PAI. In a similar manner to the broad utility of fluorescence brightness in the fluorophore design and fluorescence imaging communities, we anticipate that ALF will find broad application in comparison to PA probe potential and guide the design of improved dye-based reporters for this emerging biomedical imaging modality.

## Methods

### Instrumentation and reagents

All reagents were purchased from commercial suppliers and used without further purification. Tetrahydrofuran (THF) and diethyl ether ($Et_2O$) were obtained from a solvent purification system (MBRAUN, SPS-5). Products were purified by either normal phase flash chromatography using Merck silica gel 60 (230–400 mesh), or by reverse phase high performance liquid chromatography (HPLC) using a Waters 1525 Binary HPLC pump with a 2489 UV/Vis detector. HPLC analysis was performed with an analytical column (YMC-Pack ODS-A, 5 µm, 250 × 4.6 mm). Semi-prep HPLC purification was performed with a semi-prep column (YMC-Pack ODS-A, 5 µm, 250 × 20 mm) using 0.1% TFA buffered water and acetonitrile. Final dye products were lyophilized (Labconco™ FreeZone™ 4.5 L – 84 °C) after semi-prep HPLC.

High-resolution mass spectrometry was recorded with an Agilent 6545 Q-TOF paired with an Agilent 1260 Infinity II Prime liquid chromatography (LC) system. Mass data are reported in units of m/z. NMR spectra were recorded on a Varian VNMRS 600 MHz or Bruker Neo Nanobay 400 MHz and data were processed with MestReNova software. Chemical shifts (δ) are expressed in parts per million (ppm) and are referenced to Chloroform-*d* (7.26 ppm for $^1$H NMR, and 77.16 ppm for $^{13}$C NMR), Methanol-$d_4$ (3.31 ppm for $^1$H NMR, and 49.00 ppm for $^{13}$C NMR), Acetonitrile-$d_3$ (1.94 ppm for $^1$H NMR, and 118.26 ppm for $^{13}$C NMR), and DMSO-$d_6$ (2.50 ppm for $^1$H NMR, and 39.52 ppm for $^{13}$C NMR). $^{13}$C NMR spectra contain a persistent instrument artifact at ~187 ppm which is not from the sample. Coupling constants are reported in Hertz (Hz). Splitting patterns are indicated as follows: s, singlet; d, doublet; t, triplet; q, quartet; dd, doublet of doublet; td, triplet of doublets; dt, doublet of triplets; tt, triplet of triplets; ddd, doublet of doublet of doublets; tdd, triplet of doublet of doublets; q, quartet; m, multiplet. For $^{31}$P NMR, phosphoric acid (85 wt% in water, Sigma-Aldrich) was used as an external standard (0.00 ppm).

UV-Vis-NIR absorbance spectra were recorded with a Jasco V-780. All absorbance assays were conducted in a 3.5 mL quartz cuvette (Starna Cells) with 1 cm optical path length. UV-Vis band width was set to 2 nm, NIR band width was set to 4 nm. Response time was 0.96 s, for both UV/Vis and NIR. The scanning interval was 1 nm and the scan speed was 400 nm/min (continuous mode). Fluorescence spectra were recorded on a Fluorolog-QM (Horiba). The fluorometer was equipped with a 75 W Xenon Arc lamp with PowerArc™ lamp housing (OB-75X),

photomultiplier tube (920 PMT) detector, and a liquid nitrogen cooled indium gallium arsenide (InGaAs) detector (DSS-IGA020L/100KHZ). The sample holder was exchanged with an integrating sphere (K-Sphere) for measuring absolute quantum yields. The excitation light source could be switched to a tunable white light laser (SuperK Extreme EXU-6 PP). Fluorescence lifetimes were measured using TCSPC (Horiba). Hydrolysis of phosphinate ethyl ester dyes was measured using a Synergy H1 Hybrid Multi-Mode Reader (BioTek Instruments). Confocal images were acquired on a Leica STELLARIS 8 confocal/FLIM/tauSTED microscope system equipped with tunable white light lasers. The excitation laser was set at 755 nm with an emission PMT filter of 785–845 nm for fluorescent imaging experiments. A 405 nm diode light source with an emission PMT filter of 430–470 nm was used for nuclear stains. Images were acquired using LAS-AF software and processed in Fiji (ImageJ).

MSOT imaging was performed using an MSOT InVision 256-TF from iTheraMedical. Reported values correspond to mean PA signals in regions of interest (ROIs) of equal area unless otherwise noted. IRDye 800CW Maleimide was purchased from Li-Cor. ICG was purchased from Sigma-Aldrich. PA-HD and SiR700 were synthesized according to previously published protocols[20,44]. NU/J nude mice (002019) purchased from The Jackson Laboratory.

Graphs and statistical analysis were produced using Microsoft Excel, Graphpad Prism 10.2.0, and MATLAB R2024b. Figures were assembled using Adobe Illustrator.

### Molar extinction coefficient measurement

Dye stock solutions (10 mM) were made by dissolving the lyophilized dye powder in DMSO. Increasing concentrations of samples (1, 2, 3, 4, and 5 μM), as well as a blank (DPBS:MeCN, 7:3 with 1% DMSO), were made, and their absorbance was measured. Molar extinction coefficients were then determined by a linear fit of the absorbance versus sample concentration according to the Beer–Lambert law.

### Fluorescence emission spectra

Dye solutions were made by dissolving DMSO dye stocks in DPBS:MeCN (7:3) with 1% DMSO. Dyes were diluted to maintain the absorbance maximum below 0.1 to avoid dye re-absorption. Dye solutions were excited at the blue shoulder of the absorbance peak (typically 50 nm blue-shifted from maximum absorbance).

### Quantum yield measurement

**Absolute quantum yield measurement with integrating sphere.** The dye quantum yield obtained with an integrating sphere was measured from a dye sample (0.075 <abs <0.08) in DPBS:MeCN (7:3) with 1% DMSO. For all measurements, both excitation and emission slit widths were 2.6 nm. In short, excitation energy was measured from an emission scan of the excitation peak (for example, $\lambda_{ex} = 650$ nm, then $\lambda_{em} = 650–665$ nm) using an NDQ-200 filter to decrease the incident light. The step size was kept at 0.2 nm, and the integration time was 1 s. Emission energy was measured using an emission scan of the emission range (example 670–850 nm) with a step size of 1 nm, and an integration time of 0.5 s. A scaling factor for the NDQ filter was calculated, and, in combination with the excitation and emission scan, the quantum yield of the dye was determined using the Felix FL software QY calculator.

**Relative quantum yield measurement.** The dye quantum yield was measured from a dye sample (0.075 <abs <0.1). To compare an unknown to a reference with a known quantum yield, the following relationship was used:

$$\varphi_{sample} = \varphi_{ref}\left(\frac{m_s}{m_{ref}}\right)\left(\frac{n_s^2}{n_{ref}^2}\right)$$

Where m represents the slope of the line (y = mx + b) obtained from graphing integrated fluorescence intensity versus optical density across a series of samples, n is the refractive index of the solvent, and the subscripts s and ref represent values of the sample and reference, respectively. The relative quantum yield of $NR_{812}$ was determined by comparison to IR-1061, for which the quantum yield is 0.0041 in DCM[56].

### Measurement of fluorescence lifetimes

Fluorescence lifetimes were measured from a dye sample (0.075 <abs <0.08) in DPBS:MeCN (7:3) with 1% DMSO. Fluorescence lifetimes were determined using TCSPC with white light laser excitation at 5.556 Hz. Excitation slit widths were kept at 2 nm, and emission slit widths were kept at 5 nm, and measurement was stopped at a photon count of 10,000. A blank was measured at the appropriate wavelength from a solvent solution with 0.1% non-fat dry milk powder to provide scattering. The lifetime was calculated using Felix FL one-to-four exponentials method.

### Linear-array-based photoacoustic imaging

PAI was performed with a custom-built 3D scanning linear-array system[46]. The system employed a GE 9L-D linear-array transducer (GE Healthcare) with an optically transparent single-slit placed at the focal depth (40 mm) to enhance elevational resolution[57]. Data from the ultrasound transducer was recorded using a programmable data acquisition system (Vantage 256, Verasonics). A 30 Hz Nd:YAG laser pumping an optical parametric oscillator (Spitlight, Innolas) was used for optical excitation. The laser output was coupled into a dual-branch line fiber bundle (Dolan Jenner) that was mounted with an output on either side of the transducer aligned with the acoustic focal depth. Prior to coupling into the fiber, a beam sampler was used to direct <5% of the laser pulse energy into a power meter (Ophir), which was later used for pulse-by-pulse energy normalization. Each laser pulse has an energy of approximately 20 mJ prior to coupling into the fiber bundle. A sample stage consisting of a thin, optically and acoustically transparent membrane was placed 5 mm past the slit with water used for acoustic coupling between the transducer and membrane. The stage was scanned along the elevational axis, with one laser pulse and PA acquisition occurring at each position, and the complete 3D dataset was reconstructed following the focal line concept with a single-slit[58]. The triggering between the laser firing, ultrasound data acquisition, and sample scanning was controlled using a field-programmable gate array (myRIO, National Instruments). Drops (5 μL) of 10 μM dye samples were placed on the sample membrane, approximately aligned with the elevational axis. The samples were scanned a total of 4 cm in 0.1 mm step increments, leading to a total of 400 laser pulses, and thus ~13 s, per 3D scan. 3D scans were performed for wavelengths ranging from 694-800 nm, in 2 nm increments, leading to a total of 54 3D scans and taking a total of 12 min.

### Photoacoustic imaging with VisualSonics instrument

To verify ALF with another commercial system, combined ultrasound (US)/PA images were acquired with the Vevo F2 LAZR-X (FUJIFILM VisualSonics). The system consists of a flashlamp-pumped Q-switched Nd:YAG laser with an optical parametric oscillator for wavelength tuning (20 Hz pulse rate; ~10 ns pulse duration). Samples were imaged using the UHF29x transducer (20 Hz center frequency) with an optical fiber jacket, which secured the "narrow" optical fiber (14 mm width) to the transducer to enable simultaneous PA acquisition.

Here, a tube phantom set up[59] was utilized for US/PA imaging. Optically transparent tubes (BD IINTRAMEDIC polyethylene tubing) were secured in a 3D-printed holder. Each tube contained a different dye sample (Fig. S4a). In a plastic container (5″ × 5″ × 5″), the tube phantom was secured on top of a solidified agarose base layer (0.5% agarose + 0.2% silica; Sigma-Aldrich). The agarose base reduces

imaging artifacts by offsetting the tube phantom from highly reflective interfaces, i.e. the bottom of the plastic box or imaging table. The plastic container was then filled with water to submerge the tube phantom and couple the transducer for US/PA imaging. The transducer was positioned perpendicular to the length of the tubes to acquire circular cross-sectional images of each sample. Samples were imaged in the 680–970 nm wavelength range in 1 nm increments at the high PA sensitivity setting with zero persistence (no averaging). Data was exported to MATLAB for post-processing.

For each sample, the average PA signal was calculated for each wavelength and compiled to determine the PA spectrum. A rectangular region of interest was defined around each sample to individually analyze the PA signal. The maximum PA signal at each wavelength was determined. Due to the high frequency of pixels containing low PA signal values (Fig. S4C), only the top 80% of pixels for each wavelength were kept for analysis, i.e. pixels with PA signal less than or equal to $0.2*PA_{max}$ were set to zero. The average PA signal for each wavelength was determined by calculating the total PA signal and dividing it by the number of non-zero pixels. The process was repeated for each sample. Plots of the PA spectra were smoothed using a moving average filter of 9 wavelengths. To generate the representative histograms for IRDye 800CW, the noise floor was defined as $PA_{min} + 0.01*(PA_{max} - PA_{min})$. PA signal amplitude below the noise floor was set to zero.

### Comparison of relative hydrolysis rates

The relative hydrolysis of dyes $NR_{700}$, $NR_{735}$, $NR_{773}$, and $NR_{716}$-Cp were evaluated at 5 μM in DPBS (1% DMSO, pH 7.2) by measuring the change in absorbance at their respective absorbance maxima (700, 735, 770, and 720 nm) in 5-min intervals over 16 h. Double orbital shaking was applied for 20 s prior to each measurement. Measurements were done in triplicate at room temperature and at 37 °C. The absorbance was plotted versus time and fit to a one-phase decay exponential using GraphPad Prism.

### Cell imaging

HL-60-Luc2 cell imaging: HL-60-Luc2 cells (ATCC, CCL-240-LUC2) were grown to 80% confluency in IMDM with 20% FBS, 1x Anti-Anti, and 8 μg/mL blasticidin. For imaging, media was removed, and cells were resuspended in pre-warmed DPBS (37 °C). The cells were incubated for 20 min in DPBS with 5 μg/mL Hoechst 33342 and 10 μM $NR_{773}$. Media was removed and the cells were washed 3x with DPBS.

### Cytotoxicity assay

HL-60-Luc2 cells were plated ($1 \times 10^5$ cells/well) in a 96-well plate in IMDM (no phenol red) with 20% FBS, 1x Anti-Anti, and blasticidin (8 μg/mL) for 24 h. HL-60-Luc2 were then incubated in triplicate with 0, 10, 20, 30, 40, or 50 μM $NR_{773}$ in media for 24 h. After 24 h 10 μL CCK-8 reagent (APExBIO, K1018) was added. Absorbance was measured 4 h after incubation using a plate reader at 450 nm.

### Tissue phantom preparation

Tissue phantoms were prepared according to published protocols[60]. Briefly, tissue phantoms were prepared by dissolving agarose (10 g) in deionized water (195 mL) and 5 mL of a solution of milk made from 1 g non-fat dry milk (Boston Bioproducts Inc) and 50 mL DI $H_2O$. The mixture was heated for 2 min in a microwave, stirring every 20 s, until a translucent gel was produced. The hot gel was poured into a cylindrical mold containing an FEP tube (3 mm diameter) and cooled to room temperature for 1 h, then transferred to 4 °C for 2 h. After cooling, the phantoms were removed from the molds and cut to fit an MSOT phantom holder.

### Tissue phantom PA imaging

A solution of dye in DPBS:MeCN (7:3, with 1% DMSO) was injected into the FEP tube inserted into the cylindrical tissue phantom for imaging and the FEP tube was then sealed with hot glue. The phantom was placed into the holder and excited in 2 or 5 nm increments from 680 to 850 or 950 nm. Images were reconstructed in ViewMSOT 4.0 using the backprojection algorithm according to manufacturer procedures. Reported values correspond to mean pixel intensity values in ROIs of equal area from each sample.

For evaluation of the effects of potassium iodide addition on PA signal intensity measurements were done in DPBS (1% DMSO). In an effort to account for the donut pattern described earlier, regions of interest surrounding the entire FEP tube were selected, and the average of the top 10% of the pixel values was used for quantification.

### Calculation of signal generation efficiency

Signal generation efficiency (also known as photoacoustic generation efficiency) has been described as[43]:

$$\frac{\rho}{\mu_a}$$

Here ρ is a pressure change, i.e., photoacoustic intensity, and $\mu_a$ is molar extinction coefficient. Thus, we calculated SGE as the observed PA emission intensity at 10 μM divided by the molar extinction coefficient of the corresponding dye. All SGE values were then normalized to the SGE of $NR_{700}$, chosen as our reference for this study.

### Live-subject statement

All animal experiments were performed with the approval of the Institutional Animal Care and Use Committee (IACUC) of Virginia Commonwealth University, following principles outlined by the American Physiological Society on research animal use. Animals were housed and maintained under standard veterinary care in accordance with the AAALAC-accredited Animal Care and Use Program at Virginia Commonwealth University.

### In vivo MSOT imaging

Mice ($n = 5$) were given subcutaneous injections on the right flank above the hindlimb with either $SNR_{700}$ (100 μL of 100 μM in sterile saline containing 2% DMSO) or $NR_{773}$ (100 μL of 100 μM in sterile saline containing 2% DMSO). The mice were continuously anesthetized using isoflurane and placed in the supine position in the animal holder for imaging after injection. The temperature of the imaging chamber was set to 36 °C and the animal was allowed to equilibrate to the temperature for 10 min before imaging. Cross-sectional images were acquired from the chest to the hips of the mouse with a step size of 1 mm. The imaging position was guided by the built-in anatomy atlas in the MSOT InVision 256-TF and was kept consistent for all scans. Wavelengths used for excitation were selected based on the absorbance of $SNR_{700}$, $NR_{773}$, and endogenous absorbers (690, 700, 710, 730, 760, 770, 780, 800, 850, and 875 nm). Ten frames were recorded at every imaging wavelength. The built-in spectral unmixing feature was used to distinguish between signals coming from $SNR_{700}$ and $NR_{773}$, versus oxyhemoglobin ($HbO_2$) or hemoglobin (Hb). ROIs for each dye were determined by applying a red/blue/black color mask at either 700 nm ($SNR_{700}$) or 770 nm ($NR_{773}$). ROIs of the left and right flanks were chosen and compared to spectral unmixing to verify the localization of each dye to the ROI (Fig. S12). Integrated PA signals were determined by highlighting the full ROI for $SNR_{700}$ or $NR_{773}$, respectively, and quantifying the sum of pixel values within the ROI.

### Assessment of biodistribution and clearance of $NR_{773}$

For assessment of $NR_{773}$ clearance and accumulation, one animal was fitted with a tail vein catheter, and the animal was allowed to equilibrate to the temperature of the water bath (36 °C) for 10 min before imaging. Prior to injection, the length of the animal was imaged. Next, one position was chosen and imaged for 60 s, then 100 μL of $NR_{773}$

(100 µM in saline, 2% DMSO) was injected through the catheter, and the position was imaged for an additional 8 min. Lastly, the whole animal was imaged again.

### Reporting summary

Further information on research design is available in the Nature Portfolio Reporting Summary linked to this article.

## Data availability

The primary data generated in this study are provided in the Supplementary Information/Source Data file. Source data are provided with this paper.

## References


1. Grimm, J. B. et al. A general method to improve fluorophores for live-cell and single-molecule microscopy. *Nat. Methods* **12**, 244–250 (2015).
2. Lakowics, J. R. *Principles of Fluorescence Spectroscopy* 3rd edn. (Springer, 2007).
3. Lavis, L. D. & Raines, R. T. Bright ideas for chemical biology. *ACS Chem. Biol.* **3**, 142–155 (2008).
4. Lavis, L. D. & Raines, R. T. Bright building blocks for chemical biology. *ACS Chem. Biol.* **9**, 855–866 (2014).
5. Grimm, J. B. et al. A general method to fine-tune fluorophores for live-cell and in vivo imaging. *Nat. Methods* **14**, 987–994 (2017).
6. Zheng, Q. et al. Rational design of fluorogenic and spontaneously blinking labels for super-resolution imaging. *ACS Cent. Sci.* **5**, 1602–1613 (2019).
7. Grimm, J. B. et al. A general method to optimize and functionalize red-shifted rhodamine dyes. *Nat. Methods* **17**, 815–821 (2020).
8. Grimm, J. B. et al. Optimized red-absorbing dyes for imaging and sensing. *J. Am. Chem. Soc.* **145**, 23000–23013 (2023).
9. Wang, L. V. & Hu, S. Photoacoustic tomography: in vivo imaging from organelles to organs. *Science* **335**, 1458–1462 (2012).
10. Wang, L. V. & Yao, J. A practical guide to photoacoustic tomography in the life sciences. *Nat. Methods* **13**, 627–638 (2016).
11. Kim, C., Favazza, C. & Wang, L. V. In vivo photoacoustic tomography of chemicals: high-resolution functional and molecular optical imaging at new depths. *Chem. Rev.* **110**, 2756–2782 (2010).
12. Luke, G. P., Yeager, D. & Emelianov, S. Y. Biomedical applications of photoacoustic imaging with exogenous contrast agents. *Ann. Biomed. Eng.* **40**, 422–437 (2012).
13. Zackrisson, S., van de Ven, S. & Gambhir, S. S. Light in and sound out: emerging translational strategies for photoacoustic imaging. *Cancer Res.* **74**, 979–1004 (2014).
14. Bell, A. G. On the production and reproduction of sound by light. *Am. J. Sci.* **s3-20**, 305–324 (1880).
15. Borg, R. E. & Rochford, J. Molecular photoacoustic contrast agents: design principles & applications. *Photochem. Photobiol.* **94**, 1175–1209 (2018).
16. Weber, J., Beard, P. C. & Bohndiek, S. E. Contrast agents for molecular photoacoustic imaging. *Nat. Methods* **13**, 639–650 (2016).
17. Lucero, M. Y. & Chan, J. Photoacoustic imaging of elevated glutathione in models of lung cancer for companion diagnostic applications. *Nat. Chem.* **13**, 1248–1256 (2021).
18. Gardner, S. H. et al. A general approach to convert hemicyanine dyes into highly optimized photoacoustic scaffolds for analyte sensing. *Angew. Chem. Int. Ed.* **60**, 18860–18866 (2021).
19. Lucero, M. Y. et al. Activity-based photoacoustic probe for biopsy-free assessment of copper in murine models of Wilson's disease and liver metastasis. *Proc. Natl Acad. Sci. USA* **118**, e2106943118 (2021).
20. Lucero, M. Y. et al. Activity-based photoacoustic probes reveal elevated intestinal MGL and FAAH activity in a murine model of obesity. *Angew. Chem. Int. Ed.* **61**, e202211774 (2022).
21. Wu, Y. et al. Activatable probes for diagnosing and positioning liver injury and metastatic tumors by multispectral optoacoustic tomography. *Nat. Commun.* **9**, 3983 (2018).
22. Zhou, E. Y., Knox, H. J., Liu, C., Zhao, W. & Chan, J. A conformationally restricted Aza-BODIPY platform for stimulus-responsive probes with enhanced photoacoustic properties. *J. Am. Chem. Soc.* **141**, 17601–17609 (2019).
23. Jiang, Z. et al. Blood–brain barrier permeable photoacoustic probe for high-resolution imaging of nitric oxide in the living mouse brain. *J. Am. Chem. Soc.* **145**, 7952–7961 (2023).
24. Cui, Y. et al. A photoacoustic probe with blood-brain barrier crossing ability for imaging oxidative stress dynamics in the mouse brain. *Angew. Chem. Int. Ed.* **62**, e202214505 (2023).
25. Lucero, M. Y., East, A. K. & Chan, J. Near-infrared II photoacoustic probes for nitric oxide sensing. *Methods Enzymol.* **657**, 157–180 (2021).
26. Gao, H. et al. Boosting photoacoustic effect via intramolecular motions amplifying thermal-to-acoustic conversion efficiency for adaptive image-guided cancer. *Surg. Angew. Chem. Int. Ed.* **133**, 21215–21223 (2021).
27. Frenette, M. et al. Shining light on the dark side of imaging: excited state absorption enhancement of a bis-styryl BODIPY photoacoustic contrast agent. *J. Am. Chem. Soc.* **136**, 15853–15856 (2014).
28. Müller, M. et al. Merged molecular switches excel as optoacoustic dyes: azobenzene–cyanines are loud and photostable NIR imaging agents. *Angew. Chem. Int. Ed.* **63**, e202405636 (2024).
29. Hatamimoslehabadi, M. et al. Correlation of photophysical properties with the photoacoustic emission for a selection of established chromophores. *J. Phys. Chem. C.* **121**, 24168–24178 (2017).
30. Pownall, H. J. & Smith, L. C. Fluorescence quenching of anthracene in charged micelles by pyridinium and iodide-ions. *Biochemistry* **13**, 2594–2597 (1974).
31. Washington, K. et al. Utilization of heavy-atom effect quenching of pyrene fluorescence to determine the intramembrane distribution of halothane. *Photochem. Photobiol.* **40**, 693–702 (1984).
32. Chmyrov, A., Sandén, T. & Widengren, J. Iodide as a fluorescence quencher and promoter—mechanisms and possible implications. *J. Phys. Chem. B* **114**, 11282–11291 (2010).
33. Hanaoka, K. et al. A general fluorescence off/on strategy for fluorogenic probes: steric repulsion-induced twisted intramolecular charge transfer (sr-TICT). *Sci. Adv.* **10**, eadi8847 (2024).
34. Rathnamalala, C. S. L. et al. Xanthene-based nitric oxide-responsive nanosensor for photoacoustic imaging in the SWIR window. *Angew. Chem. Int. Ed.* **62**, e202214855 (2023).
35. Zhou, X., Fang, Y., Wimalasiri, V., Stains, C. I. & Miller, E. W. A long-wavelength xanthene dye for photoacoustic imaging. *Chem. Commun.* **58**, 11941–11944 (2022).
36. Brøndsted, F. et al. Single atom stabilization of phosphinate ester-containing rhodamines yields cell permeable probes for turn-on photoacoustic imaging. *Chem. Eur. J.* **30**, e202303038 (2023).
37. Zhou, X., Lai, R., Beck, J. R., Li, H. & Stains, C. I. Nebraska red: a phosphinate-based near-infrared fluorophore scaffold for chemical biology applications. *Chem. Commun.* **52**, 12290–12293 (2016).
38. Zhou, X., Fang, Y., Lesiak, L. & Stains, C. I. A phosphinate-containing fluorophore capable of selectively inducing apoptosis in cancer cells. *Chembiochem* **20**, 1712–1716 (2019).
39. Fang, Y., Good, G. N., Zhou, X. & Stains, C. I. Phosphinate-containing rhodol and fluorescein scaffolds for the development of bioprobes. *Chem. Commun.* **55**, 5962–5965 (2019).
40. Lesiak, L. et al. Imaging GPCR internalization using near-infrared Nebraska red-based reagents. *Org. Biomol. Chem.* **18**, 2459–2467 (2020).
41. Yin, R. W. et al. Azaphosphinate dyes: a low molecular weight near-infrared scaffold for development of photoacoustic or fluorescence imaging probes. *Chem. Eur. J.* **30**, e202303331 (2024).

42. DiMeglio, D. et al. Experimentally calibrated computational prediction enables accurate fine-tuning of near-infrared rhodamines for multiplexing. *Chem. Eur. J.* **29**, e202202861 (2023).
43. Fuenzalida Werner, J. P. et al. Challenging a preconception: optoacoustic spectrum differs from the optical absorption spectrum of proteins and dyes for molecular imaging. *Anal. Chem.* **92**, 10717–10724 (2020).
44. Koide, Y. et al. Development of NIR fluorescent dyes based on Si–rhodamine for in vivo imaging. *J. Am. Chem. Soc.* **134**, 5029–5031 (2012).
45. Friedman, H. C. et al. Establishing design principles for emissive organic SWIR chromophores from energy gap laws. *Chem* **7**, 3359–3376 (2021).
46. Menozzi, L. et al. Three-dimensional diffractive acoustic tomography. *Nat. Commun.* **16**, 1149 (2025).
47. Reinhardt, C. J., Xu, R. & Chan, J. Nitric oxide imaging in cancer enabled by steric relaxation of a photoacoustic probe platform. *Chem. Sci.* **11**, 1587–1592 (2020).
48. Myochin, T. et al. Development of a series of near-infrared dark quenchers based on Si-rhodamines and their application to fluorescent probes. *J. Am. Chem. Soc.* **137**, 4759–4765 (2015).
49. Ikeno, T. et al. Design and synthesis of an activatable photoacoustic probe for hypochlorous acid. *Anal. Chem.* **91**, 9086–9092 (2019).
50. Kuimova, M. K., Yahioglu, G., Levitt, J. A. & Suhling, K. Molecular rotor measures viscosity of live cells via fluorescence lifetime imaging. *J. Am. Chem. Soc.* **130**, 6672–6673 (2008).
51. Ren, T. B. et al. A general method to increase Stokes shift by introducing alternating vibronic structures. *J. Am. Chem. Soc.* **140**, 7716–7722 (2018).
52. Morgounova, E., Shao, Q., Hackel, B., Thomas, D. & Ashkenazi, S. Photoacoustic lifetime contrast between methylene blue monomers and self-quenched dimers as a model for dual-labeled activatable probes. *J. Biomed. Opt.* **18**, 056004 (2013).
53. Widengren, J., Mets, U. & Rigler, R. Fluorescence correlation spectroscopy of triplet states in solution: a theoretical and experimental study. *J. Phys. Chem.* **99**, 13368–13379 (1995).
54. Klymchenko, A. S. Solvatochromic and fluorogenic dyes as environment-sensitive probes: design and biological applications. *Acc. Chem. Res.* **50**, 366–375 (2017).
55. Haidekker, M. A. & Theodorakis, E. A. Molecular rotors—fluorescent biosensors for viscosity and flow. *Org. Biomol. Chem.* **5**, 1669–1678 (2007).
56. Hoshi, R., Suzuki, K., Hasebe, N., Yoshihara, T. & Tobita, S. Absolute quantum yield measurements of near-infrared emission with correction for solvent absorption. *Anal. Chem.* **92**, 607–611 (2020).
57. Wang, Y. et al. Slit-enabled linear-array photoacoustic tomography with near isotropic spatial resolution in three dimensions. *Opt. Lett.* **41**, 127–130 (2016).
58. Xia, J. et al. Three-dimensional photoacoustic tomography based on the focal-line concept. *J. Biomed. Opt.* **16**, 090505 (2011).
59. Jhunjhunwala, A., Kim, J., Kubelick, K. P., Ethier, C. R. & Emelianov, S. Y. In vivo photoacoustic monitoring of stem cell location and apoptosis with caspase-3-responsive nanosensors. *ACS Nano* **17**, 17931–17945 (2023).
60. Knox, H. J. et al. A bioreducible N-oxide-based probe for photoacoustic imaging of hypoxia. *Nat. Commun.* **8**, 1794 (2017).


## Acknowledgements

F.B. was supported by a Mary Anderson Harrison Jefferson Fellowship from the Jefferson Scholars Foundation. The MSOT data included in this study was generated at the Bioimaging and Applied Research Core facility at Virginia Commonwealth University. We thank Joshua Mitchell and Frank Corwin for their assistance with live animal imaging experiments. We thank the Biomolecular Magnetic Resonance Facility, the Hi-Resolution Mass Spectrometer Facility, and we acknowledge the W. M. Keck Center for Cellular Imaging for the use of the Leica STELLARIS 8 confocal/FLIM/tauSTED microscope system (NIH OD030409). We acknowledge financial support from the NIH (R35GM148221: C.I.S.; R01NS111039, R01DK139109, R01HL166522, and R01GM134036: J.Y.), NSF (2144788: J.Y. and DGE-2139754: L.M.), Duke Coulter Translational Grant (J.Y.), North Carolina Biotechnology Center Triangle Research Grant (2024-TRG-0041: J.Y.), University of Virginia Biomedical Engineering Department (K.P.K.), and the University of Virginia (C.I.S.). The content of this work is solely the responsibility of the authors and does not necessarily represent the official views of the NIH.

## Author contributions

C.I.S. and F.B. designed the study. F.B. and J.L.M. led the experiments and data analysis. F.B., J.L.M., J.D.M., H.R.S., X.Z., and R.Y. contributed to dye synthesis and characterization. L.M. and J.Y. performed PAI on a custom-built 3D scanning linear-array system and performed data analysis. Y.F. assisted with data analysis. K.P.K. performed PAI and data analysis on a Fujifilm VisualSonics instrument. F.B. and C.I.S. wrote the manuscript with input from all authors.

## Competing interests

L.M. and J.Y. have financial interests with Lumius Imaging, Inc., which did not support this work. F.B., X.Z, Y.F., and C.I.S. have filed a patent covering phosphinate dyes. The remaining authors declare no competing interests.

## Additional information

**Supplementary information** The online version contains supplementary material available at https://doi.org/10.1038/s41467-025-59121-6.

**Correspondence** and requests for materials should be addressed to Cliff I. Stains.

**Peer review information** *Nature Communications* thanks Maged Henary and the other, anonymous, reviewer(s) for their contribution to the peer review of this work. A peer review file is available.